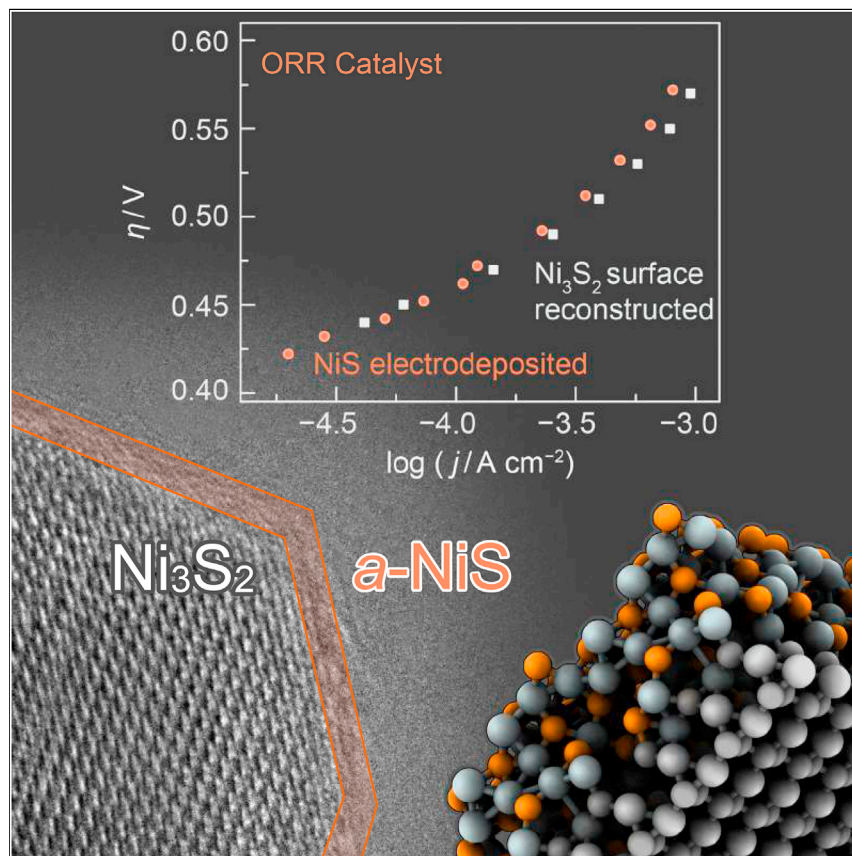


Article

Surface Restructuring of Nickel Sulfide Generates Optimally Coordinated Active Sites for Oxygen Reduction Catalysis



Crystalline Ni₃S₂ oxygen reduction reaction (ORR) catalysts undergo oxidative surface reconstruction under catalytic conditions to generate an approximately 2 nm amorphous surface layer with NiS stoichiometry. DFT calculations establish a simple local coordination number based descriptor for ORR catalysis and suggest that Ni atoms surrounded by three S nearest neighbors display optimal activity. The surface reconstructed Ni₃S₂ exhibits similar ORR activity to electrodeposited amorphous NiS films.

Bing Yan, Dilip Krishnamurthy,
Christopher H. Hendon,
Siddharth Deshpande, Yogesh
Surendranath,
Venkatasubramanian
Viswanathan

yogi@mit.edu (Y.S.)
venkvis@cmu.edu (V.V.)

HIGHLIGHTS

The ORR catalyst Ni₃S₂ undergoes surface reconstruction under catalytic conditions

Surface reconstruction generates a highly active amorphous surface NiS phase

The local coordination environment of Ni surface sites determines ORR activity

A simple coordination number descriptor holds for ORR on nickel sulfide catalysts

Article

Surface Restructuring of Nickel Sulfide Generates Optimally Coordinated Active Sites for Oxygen Reduction Catalysis

Bing Yan,^{1,3} Dilip Krishnamurthy,^{2,3} Christopher H. Hendon,¹ Siddharth Deshpande,² Yogesh Surendranath,^{1,4,*} and Venkatasubramanian Viswanathan^{2,*}

SUMMARY

The Ni_3S_2 bulk phase supports efficient oxygen reduction reaction (ORR) catalysis in pH neutral aqueous electrolytes. Here, we combine electrochemistry, surface spectroscopy, and high-resolution microscopy to show that Ni_3S_2 undergoes self-limiting oxidative surface restructuring under ORR conditions to form an amorphous surface film conformally coating the Ni_3S_2 crystallites. The surface film has a nominal NiS stoichiometry and is highly active for ORR catalysis. Density functional theory calculations suggest that, to a first approximation, the catalytic activity of nickel sulfides is determined by the Ni-S coordination numbers at surface-exposed sites through a simple geometric descriptor. In particular, Ni surface sites with three S nearest neighbors, formed via reconstruction of the Ni_3S_2 surface, provide an optimal energetic landscape for ORR catalysis. By providing a framework for understanding catalytic activity on reconstructed amorphous surface phases, the work enables the rational design of high-performance electrocatalysts based on kinetically labile, earth-abundant materials.

INTRODUCTION

The interconversion of water and oxygen is a central chemistry underlying the storage of renewable electricity in energy-dense chemical bonds.¹ The oxidation of H_2O to O_2 is the efficiency-limiting half reaction for the splitting of water to generate H_2 fuel, whereas the reduction of O_2 to H_2O is the efficiency-limiting cathode reaction in low-temperature fuel cells.² Platinum group metals and their corresponding oxides and chalcogenides are well-known catalysts for these reactions,^{3,4} but recent studies have uncovered a diversity of earth-abundant first-row transition metal oxides^{5,6} and chalcogenides^{7,8} that, depending on the reaction conditions, rival the activity of their precious metal analogs.

Unlike their precious metal congeners, first-row transition-metal ions are labile,^{9,10} and as a result, the surfaces of these materials are expected to be more dynamic under the conditions of catalysis. Indeed, the remarkable propensity for first-row transition-metal oxides to reconstruct and in many cases amorphize under the condition of the oxygen evolution reaction (OER) has been well documented.^{11–13} Understanding these surface dynamics is critical for developing rigorous structure-function correlations, because the surface phase rather than the bulk precatalyst carries out the desired reaction. However, compared with the rich contemporary understanding of surface phase transformations under OER conditions, there exists a paucity of information about the analogous dynamics that give rise to active surface phases for

Context & Scale

In heterogeneous catalysis, only the surface of the active material is responsible for catalytic turnover. These surfaces often undergo dynamic changes that lead to altered structures and compositions relative to the bulk of the material. Thus, the development of improved catalysts requires a detailed understanding of these surface dynamics under the conditions of the reaction. Here, we uncover these dynamics on an earth-abundant catalyst, Ni_3S_2 , that is highly active for the conversion of oxygen to water, the efficiency-limiting reaction in low-temperature fuel cells. We demonstrate that the surface of this material transforms into a disordered and active ~ 2 nm NiS layer. We establish that the activity of materials of this type can be estimated by simply considering the number of S atoms directly bonded to the Ni active sites on the surface. This simple geometric descriptor enables the rational design of the disordered structures that persist on many catalytically active surfaces.

the oxygen reduction reaction (ORR). In part, this is due to the limited number of heterogeneous ORR catalysts containing first-row transition-metal ions. Pt alloys of Ni and Co present a notable exception. For these alloys, the labile first-row transition-metal component undergoes oxidative dissolution, leaving behind Pt-rich skins that display enhanced ORR activity.^{14,15} For Ru-based chalcogenide, Ru_xSe_y , *in situ* grazing incidence X-ray absorption studies revealed surface distortion of the primary coordination environment of Ru centers under ORR conditions.¹⁶ Despite these precedents, the surface phase dynamics of noble-metal-free ORR catalysts remain almost entirely unexplored despite the expectation that they would be even more susceptible to surface reconstruction under catalytic conditions.

First-row late transition metal chalcogenides (LTMCs) containing Fe, Co, and Ni have been identified as a potent class of catalysts for the ORR.^{17,18} The best-performing LTMCs exhibit ORR onset potentials in the range of 0.7–0.8 V versus the reversible hydrogen electrode (RHE), requiring only ~0.1 V greater overpotential than Pt. In addition to being composed entirely of low-cost, earth-abundant elements, LTMCs display excellent tolerance to crossover of fuels such as methanol and common fuel contaminants such as CO, making them particularly promising as low-cost materials for next-generation low-temperature fuel cell technologies.¹⁹ Despite their attractive qualities, the systematic improvement of the performance of these materials has been impeded by a lack of coherent structure-function correlations that can be used as the basis for rational catalyst design. Indeed, there remains a great deal of ambiguity about the surface structures that are responsible for catalysis because of the paucity of investigations that examine surface phase dynamics under catalytically relevant conditions.²⁰

Recently, we reported that the heazlewoodite, Ni_3S_2 , bulk phase supports efficient ORR catalysis under benign neutral pH conditions.²¹ The material displays superior performance relative to the corresponding first-row transition-metal oxides with an ORR onset potential of 0.80 V and, unlike Pt, is remarkably tolerant to poisoning by electrolyte ions such as phosphate. These properties, combined with the known tolerance of LTMCs to common liquid fuels, such as formate, make this material particularly attractive for low-cost, membrane-free fuel cells.^{22–24} In order to enable the systematic development of improved earth-abundant ORR catalysts, we now probe the surface phase dynamics of this material to identify the active surface structures. We find that the surface layers of Ni_3S_2 undergo a self-limiting oxidative reconstruction under ORR conditions to generate a conformal ~2-nm-thick amorphous nickel sulfide surface layer with an approximate stoichiometry of Ni:S 1:1. We show via independent synthesis that this amorphous surface phase can account for the high catalytic activity of Ni_3S_2 for the ORR under neutral pH conditions.

In order to probe the diverse surface chemistry that emerges upon reconstruction, we performed density functional theory (DFT) calculations for ORR on several crystalline and amorphous nickel sulfide phases. Our analysis indicates that to a first approximation, the key activity descriptor for ORR, the free energy of adsorbed OH^* , is determined by the local bonding environment of surface-exposed Ni sites and dominated by their nearest-neighbor sulfur coordination number. We find that surface Ni sites that have three sulfur neighbors possess optimal activity, and such sites exist at the surfaces of several nickel sulfide phases. Furthermore, the same geometric descriptor is found to hold for amorphous layers with NiS stoichiometry. We apply these observations to show that the restructured amorphous surface layer hosts optimally coordinated Ni sites primed for efficient ORR catalysis. This work highlights the central role of surface reconstructions in defining catalytic

¹Department of Chemistry, Massachusetts Institute of Technology, 77 Massachusetts Avenue, Cambridge, MA 02139-4307, USA

²Department of Mechanical Engineering, Carnegie Mellon University, 5000 Forbes Avenue, Pittsburgh, PA 15213, USA

³These authors contributed equally

⁴Lead Contact

*Correspondence: yogi@mit.edu (Y.S.), venkvis@cmu.edu (V.V.)

<http://dx.doi.org/10.1016/j.joule.2017.08.020>

performance, particularly on kinetically labile earth-abundant materials, and provides a descriptor-based approach for identifying the most active sites on the reconstructed surface phase. Knowledge of these active structures and the surface transformations that give rise to them enables the rational design of new material classes for earth-abundant ORR catalysis.

RESULTS AND DISCUSSION

The Ni-S phase diagram consists of six stoichiometric nickel sulfide phases, which range in composition from Ni_3S_2 to NiS_2 .²⁵ The heazlewoodite end member phase, Ni_3S_2 , examined in this study, crystallizes in the trigonal space group R32 with each Ni bound to four S and four Ni nearest-neighbor atoms (Figure S1A). The Ni-Ni bonds in Ni_3S_2 are 2.50 Å, only slightly longer than the corresponding bond length of 2.44 Å observed in Ni metal. We synthesized Ni_3S_2 by combining Ni and S powder in a stoichiometric ratio, followed by heating under vacuum in a sealed quartz tube at 600°C for 20 hr and then at 800°C for another 4 hr.²⁶ Powder X-ray diffraction (Figure S1B) of this material reveals peaks corresponding only to heazlewoodite Ni_3S_2 ,²⁷ evincing the formation of a phase-pure sample. Transmission electron microscopy (TEM) and scanning electron microscopy (SEM) reveal average crystallite dimensions of several hundred nanometers (Figure S2).

The surfaces of the as-prepared Ni_3S_2 samples are structurally similar to the bulk lattice. In line with literature reports, X-ray photoelectron spectroscopy (XPS) of the as-synthesized Ni_3S_2 shows a Ni 2p_{3/2} peak at 852.7 eV, and S 2p peak at 162.5 eV²⁸ (Figures 1A and 1B, black) in a 3:2 atomic ratio, along with an adventitious O peak of low intensity at 531.8 eV. In addition, high-resolution TEM images of Ni_3S_2 particles uniformly display lattice fringes that extend to the edge of each crystallite (Figures S3A and S3B). Together, these data indicate that the surfaces of Ni_3S_2 particles remain crystalline and are not subject to significant deterioration prior to the electrochemical investigations detailed below.

The surfaces of Ni_3S_2 undergo self-limiting oxidative phase conversion under electrochemical polarization. Freshly prepared Ni_3S_2 particulates were pressed onto gold electrodes and examined by cyclic voltammetry (CV) in N₂-saturated 1 M sodium phosphate (NaP_i) electrolyte (pH 7). Consistent with Ni_3S_2 having a formal Ni valency of 4/3, we observed a low open-circuit potential of 0.30 V (all potentials are reported versus RHE). Scanning negative of this value reveals no discernable CV features up to 0.00 V. However, on the first positive going scan, we observe a large irreversible oxidative wave with a peak potential of $E_{p,a} = 0.47$ V (Figure 1D). Notably, the peak of this oxidative feature resides ~0.30 V negative of the onset potentials for ORR on the Ni_3S_2 material. Upon scanning positive of the anodic peak, the current rapidly declines, reaching a background level with no additional oxidative features up until 0.9 V. Importantly, this oxidative peak is not accompanied by any reductive features on the subsequent negative going scan and the magnitude of the oxidative peak rapidly declines in subsequent scans and is not detectable by the seventh CV cycle of a freshly prepared electrode. Together, the electrochemical data establish that Ni_3S_2 surfaces undergo irreversible self-limiting oxidation under electrochemical polarization to the potentials necessary for ORR catalysis.

XPS of the CV-cycled Ni_3S_2 electrode reveals a reconstructed surface with a reduced Ni stoichiometry. On the surface, the Ni 2p_{3/2} peak shifts slightly to higher binding energy from 852.7 to 853.0 eV, and we observe a small peak at 856.0 eV corresponding to a minority surface population of Ni(OH)_2 (Figure 1A, red).^{28,29} In addition, the

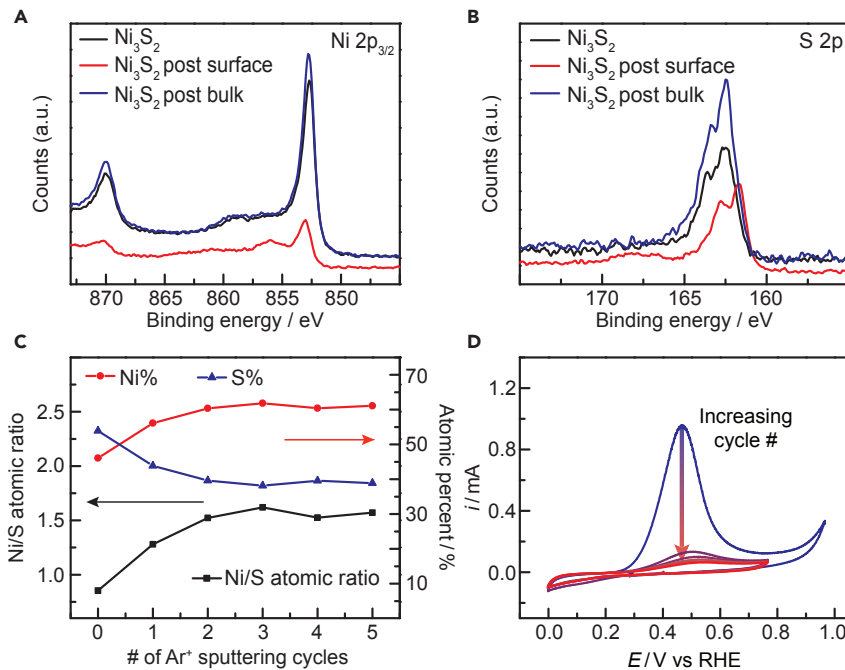


Figure 1. XPS and Electrochemical Characterization of Ni₃S₂ Surface Reconstruction

(A and B) High-resolution XPS of (A) Ni 2p_{3/2} and (B) S 2p regions. As-prepared Ni₃S₂, post-oxidation surface, and bulk Ni₃S₂ are shown in black, red, and blue, respectively.

(C) XPS-derived Ni and S atomic ratios and percentages as a function of the number of Ar⁺ sputtering cycles.

(D) Initial CV scans of Ni₃S₂ recorded in N₂-saturated 1 M sodium phosphate electrolyte (pH 7), at a scan rate of 5 mV s⁻¹ and rotation rate of 2,000 rpm.

See also Figure S4.

S 2p peak shifts from 162.5 to 161.7 eV, similar to the peak position observed for NiS (Figure 1B, red).^{28,30} Following surface reconstruction, we observe a Ni:S atomic ratio of 0.9:1.0 (Figure 1C). We also observe an O 1s peak at 531.60 eV (Figure S4, blue) attributed to a minority surface population of Ni(OH)₂ or surface-adsorbed hydroxide species.²⁹ Following argon ion (Ar⁺) etching of the surface, the peak positions of Ni and S both return to the values typical of Ni₃S₂ and the O peak disappears (Figures 1A and 1B, blue; Figure S4, red and black). The Ni:S atomic ratio increases to 1.3:1.0 and 1.5:1.0 after one and two cycles of Ar⁺ sputtering, respectively. The value stabilizes at ~1.5:1.0, in line with the bulk stoichiometry of Ni₃S₂ (Figure 1C). Together, the XPS results reveal that the surfaces of Ni₃S₂ undergo oxidative reconstruction upon CV cycling in neutral electrolyte to form a new surface phase with an approximate empirical formula of NiS.

High-resolution TEM (HRTEM) images suggest that the surface phase conversion is accompanied by morphological changes. As the solid-state synthesis described above produced particles too large (a few hundred nanometers) to discern changes in nanoscale morphology, we prepared Ni₃S₂ nanoparticles following a procedure adapted from the literature³¹ and used these samples for HRTEM investigations. Similar to the solid-state prepared samples, the as-prepared nanoparticles display uniform Ni₃S₂ lattice fringes extending to the edge of each crystallite (Figures 2A, S3C, and S3D). These nanoparticles were affixed to a TEM grid and subjected to potential cycling as described above until the oxidative peak declined to the background level. Following this electrochemical treatment, we observed a thin

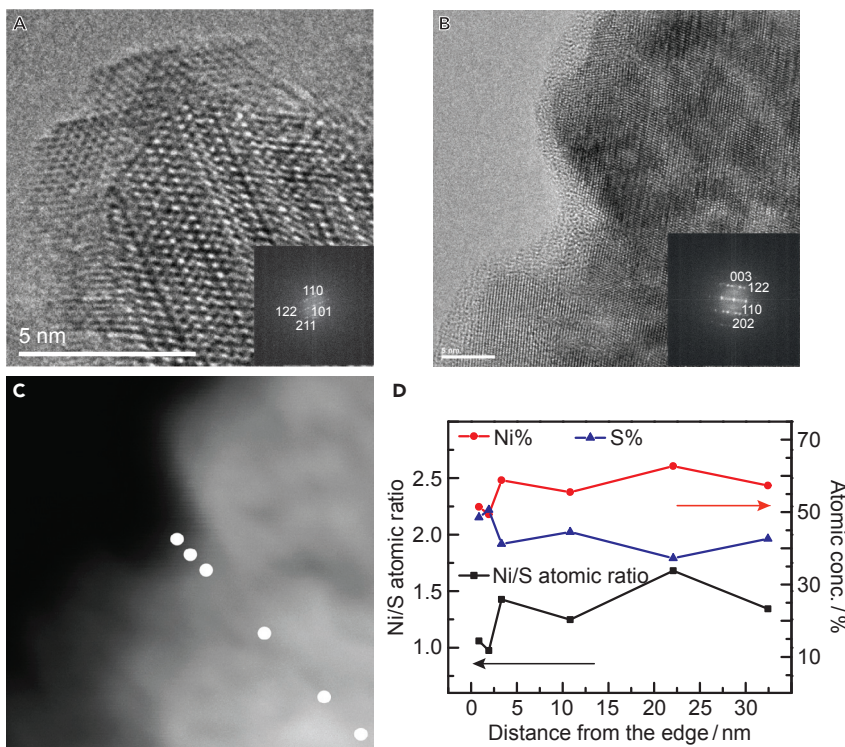


Figure 2. TEM Characterization of Surface-Restructured Ni_3S_2

(A and B) TEM images of (A) as-prepared and (B) post-electrolysis Ni_3S_2 nanoparticles. Fast Fourier transforms are shown in the insets of (A) and (B) and confirm the crystalline nature of the bulk material. The scale bars are 5 nm.

(C and D) Elemental composition determined from energy-dispersive X-ray spectroscopy (EDS) at a series of spots along a line from the crystallite edge to the bulk (C) reveals the variation in Ni:S composition across the crystallite (D).

See also Figures S3 and S5.

amorphous “shell” conformally coating each particle (Figures 2B and S5). By sampling the shell thickness across ten particles, we obtained a histogram showing an average shell thickness of 1.6 ± 0.6 nm (Figures S6A and S6B). To gain more insight into this self-limiting surface phase transformation, we performed chronoamperometry (CA) in O_2 -saturated neutral electrolyte on the freshly prepared Ni_3S_2 nanoparticles. At 0.71 V, we observed an initial anodic current corresponding to oxidative restructuring, which rapidly decays to a steady-state cathodic value corresponding to ORR catalysis (Figure S6C). The histograms of the amorphous surface layer thickness after 23 s (immediately prior to the onset of net cathodic current), 2 min, and 5 min of CA polarization (Figures S6D–S6F) reveal an average amorphous layer thickness of 1.5 ± 0.7 , 2.0 ± 0.9 and 1.9 ± 0.4 nm, respectively. Prolonged polarization beyond these time points does not lead to any further changes in the thickness of the amorphous layer, consistent with the self-limiting nature of the oxidative restructuring. To further probe this self-limiting surface restructuring, we performed pH-dependence studies by recording CVs on freshly prepared Ni_3S_2 electrodes in pH 4.68, 7.02, 8.37, and 9.87 sodium phosphate electrolyte (Figure S7, details are discussed in the [Supplemental Information](#)). The experimental data are in line with the Pourbaix diagram (Figure S8 and Table S1) we constructed from the thermodynamic data of known nickel compounds, further substantiating the formation of amorphous NiS (a-NiS) upon electrochemical cycling at neutral pH. Together, the data indicate

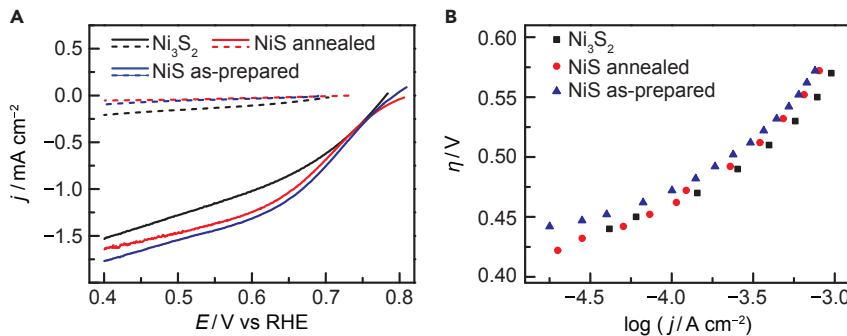


Figure 3. ORR Activity of Ni_3S_2 and Electrodeposited NiS

(A and B) Linear sweep (5 mV s^{-1} scan rate) voltammograms (LSVs) (A) and Tafel plots (B) of Ni_3S_2 (black), as-prepared NiS (blue), and annealed NiS (red). LSVs (A, solid lines) and steady-state measurements (B) were recorded in O_2 -saturated 1 M sodium phosphate electrolyte (pH 7), at a rotation rate of 2,000 rpm. LSVs recorded in N_2 -saturated electrolyte are plotted in dashed lines. See also Figures S11–S13.

that the surface reconstruction of Ni_3S_2 generates an amorphous $\sim 2.0 \text{ nm}$ a-NiS surface layer that serves to passivate the Ni_3S_2 host from further oxidation.

Energy-dispersive X-ray spectroscopy (EDS) under scanning transmission electron microscopy mode further confirms a Ni:S composition change in the thin surface amorphous layer. EDS data were collected at a variety of points extending from the edge of the nanoparticle to its interior (Figure 2C), and the corresponding Ni:S atomic ratio is plotted in Figure 2D. At the edge of the particle, where the amorphous layer is present, the Ni:S atomic ratio is $\sim 1.0:1.0$, and this ratio rapidly increases to $\sim 1.5:1.0$ as the scan proceeds to the interior of the Ni_3S_2 particle, reflecting the bulk stoichiometry. These TEM data, combined with the electrochemical and XPS data described above, indicate that the surfaces of Ni_3S_2 undergo oxidative restructuring at the potentials necessary for ORR catalysis, forming an amorphous $\sim 2 \text{ nm}$ layer with a nominal NiS stoichiometry.

To determine whether the amorphous surface layer is the active phase, we compared the ORR activity of surface-restructured Ni_3S_2 with independently prepared crystalline and amorphous NiS. We electrodeposited NiS on an Au RDE substrate using a method adapted from previous reports.^{32,33} The as-prepared NiS film was amorphous as judged by the absence of peaks in grazing incidence diffractograms (Figure S10A). Following thermal annealing at 250°C under N_2 for 3 hr, the crystallinity of the film is improved and grazing incident XRD (GIXD) and XPS evince the formation of crystalline NiS surface phases (Figures S10B–S10D). The ORR activity of these materials was assessed in O_2 -saturated 1 M NaPi (pH 7). The as-prepared Ni_3S_2 electrode undergoes surface oxidation in the first several CV scans while simultaneously catalyzing ORR (Figure S9). The anodic peaks corresponding to this oxidative surface reconstruction are observed at the same potential as observed in the absence of O_2 (Figure 1D), and upon completion of the surface self-limiting reconstruction, the film displays robust ORR catalysis with an onset potential (defined as the potential corresponding to -0.1 mA cm^{-2} geometric current density) of 0.77 V (Figure 3A). Unlike Ni_3S_2 , initial CV scans of as-prepared and thermally annealed NiS display no oxidative features and are active for ORR catalysis with an onset potential of 0.78 V, very similar to that of Ni_3S_2 upon surface transformation. Steady-state chronoamperograms for Ni_3S_2 and as-prepared and annealed NiS were recorded at various applied potentials to construct Tafel plots of

overpotential versus the logarithm of the activation-controlled current density (Figure 3B). Tafel plots for Ni_3S_2 , as-prepared NiS, and annealed NiS samples nearly overlay over the entire 1.5 decade range of Tafel data collection, and the steady-state data are comparable with the linear sweep voltammograms (Figure S11), illustrating the similarity in these samples' intrinsic ORR activities. Indeed, the slightly higher activity of Ni_3S_2 at lower overpotentials may be explained by a slightly higher electroactive surface area relative to NiS (Figure S12). At higher overpotentials, the Tafel slopes for Ni_3S_2 and electrodeposited NiS rise, explaining why the current does not reach the mass-transport-limited value (Figure S13). Together, these data indicate that the Ni_3S_2 undergoes an oxidative transformation to generate an active amorphous surface phase of nominal NiS stoichiometry.

The high activity of the amorphous surface films raises interest in identifying the nature of the specific active sites responsible for ORR catalysis. Given the rich Ni-S phase diagram, we expect a wide variety of possible active sites, especially in the amorphous surface layer, and thus, it is necessary to develop general principles that connect local structure to electrocatalytic activity. In order to probe the possible active sites, we initially performed DFT calculations of ORR activity on low-index facets of several crystalline nickel sulfide phases: NiS_2 , Ni_3S_4 , NiS, Ni_9S_8 , Ni_3S_2 (Figure S14). The spectrum of local active site structures on these crystalline nickel sulfide phases and their corresponding calculated electrocatalytic activity were used to formulate a correlation between the local coordination of active sites and their associated ORR activity. This correlation was used to probe the origin of the high activity of the restructured amorphous surface phase.

In the associative mechanism for ORR, the initial reduction of O_2 leads to OOH^* (* represents adsorbed species) and subsequent oxygen-oxygen bond cleavage yields O^* and OH^* , which are reduced to water.³⁴ The electrocatalytic activity for ORR is thus determined by the free energies of adsorption of OOH^* , OH^* and O^* . We computed the adsorption free energies of these intermediates on the known crystalline phases of the nickel sulfide family (Figures S23–S27; Table S3). The effect of solvation has led to improved predictions of activity for oxygen reduction and evolution, largely building on the foundational understanding developed on interaction of water on metal surfaces.^{35–39} The understanding of the interaction of water with other classes of materials is limited, and in the case of sulfides, a precise solvation structure of water and oxygen intermediates is not well established. Thus, there is a need to develop a fundamental understanding of the interaction between sulfides and water-hydroxyl layers, which requires a concerted theoretical and experimental effort leveraging both ab initio molecular dynamics and X-ray spectroscopy.⁴⁰ In the absence of a validated model for solvation at metal sulfide surfaces, we make the simplifying assumption that its effect is minimal in describing trends in adsorption energy for these materials.

We observe scaling between the adsorption energies of OOH^* and OH^* on the various Ni-S phases. The scaling has a slope of 1 with an intercept close to 3.04, as shown in Figure 4A. The slope of 1 is the same as that observed on metallic surfaces^{41,42}, nanoparticles,⁴³ and various transition-metal compounds such as oxides, carbides, nitrides, and sulfides,⁴⁴ and can be rationalized based on bond-order conservation principles^{45,46}. It is worth emphasizing that the intercept of the scaling relation differs depending on the degree of solvation around the intermediates.⁴⁷ On metal surfaces, water stabilizes OH^* much more relative to OOH^* ; on oxide surfaces, however, there is no additional stabilization for either OOH^* or OH^* . As would be expected, the calculated intercept is close to that observed on oxide surfaces.⁴⁸

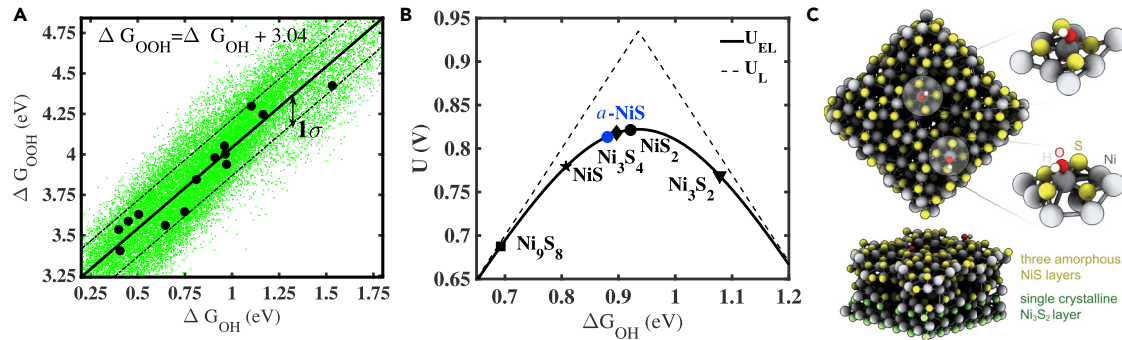


Figure 4. ORR Activity Predictions Based on DFT Calculations

(A) Scaling between adsorption free energies of OH^* and OOH^* on the various stable Ni-S phases. The black dots represent the adsorption energies and the green dots represents the ensemble of adsorption free energies obtained from the BEEF-vdW functional that enables error estimation. The best-fit line is given by $\Delta G_{\text{OOH}^*} = \Delta G_{\text{OH}^*} + 3.04$, and the intercept has a standard deviation of 0.17 eV. The black dotted lines represent the 1σ lines. (B) ORR activity volcano of nickel sulfide phases showing the expected limiting potential (bold line) and the limiting potential (dashed line) obtained from a thermodynamic analysis, as a function of the DFT-calculated adsorption free energy of the intermediate OH^* . The analysis suggests that multiple Ni-S phases exhibit very high ORR activity (Ni_3S_2 , NiS , Ni_3S_4 , and $a\text{-NiS}$). $a\text{-NiS}$ represents the amorphous Ni:S 1:1 phase. (C) $a\text{-NiS}$ structure constructed from *ab initio* simulated annealing.

An important consequence of scaling is that the activity is governed by the free energy of one reaction intermediate,^{49–51} chosen to be the free energy of OH^* for this study. From the reaction free energies for the associative mechanism, we can determine the limiting potential, U_L , which is the highest potential at which the reaction mechanism is downhill in free energy. This thermodynamic approach has been used successfully in understanding trends in activity⁵² and selectivity^{53,54} in oxygen reduction and oxygen evolution.⁴⁹ Using scaling, we can plot the limiting potential, U_L , as a function of the adsorption energy of OH^* , ΔG_{OH^*} , and is shown in Figure 4B. The strong-binding (left) leg is determined by the removal of OH^* and the weak-binding leg is determined by activation of O_2 as OOH^* . A recently developed exchange correlation functional, Bayesian Error Estimation Functional with van der Waals correlation (BEEF-vdW),⁵⁵ allows for estimating uncertainty in the predicted limiting potentials,⁵⁶ and a more detailed description of the approach is given in the *Supplemental Information* (Figures S15–S17). Using this approach, a quantity known as the expected limiting potential, U_{EL} , can be extracted, which gives the value of the limiting potential taking into account the uncertainty associated with DFT calculations.

Based on DFT calculations, we find that $\text{Ni}(111)$ binds OH^* very strongly and lies on the strong-binding leg. The addition of sulfur leads to a weakening of OH^* bonding to the active sites, which we find are the Ni centers. The DFT-computed adsorption free energy of OH^* for the various Ni-S phases is shown in Figure 4B, and we find that several phases possess surface sites that have high activity. This raises the important question of what common structural features exist among these surface sites. In order to probe these features, we analyzed the structural environment around the active site in search of a structure-energy-activity descriptor. Such descriptors have been identified for metal electrocatalysts for ORR^{57–60} and recently for transition-metal oxides.⁶¹

We characterized the local environment of active sites through the coordination numbers of nearest-neighboring nickel and sulfur atoms, CN_{Ni} and CN_{S} . We constructed the simplest possible model that linearly depends on these coordination numbers, i.e., $\Delta G_{\text{OH}} = \alpha_1 \text{CN}_{\text{Ni}} + \alpha_2 \text{CN}_{\text{S}}$. We then carried out a least-squares fit

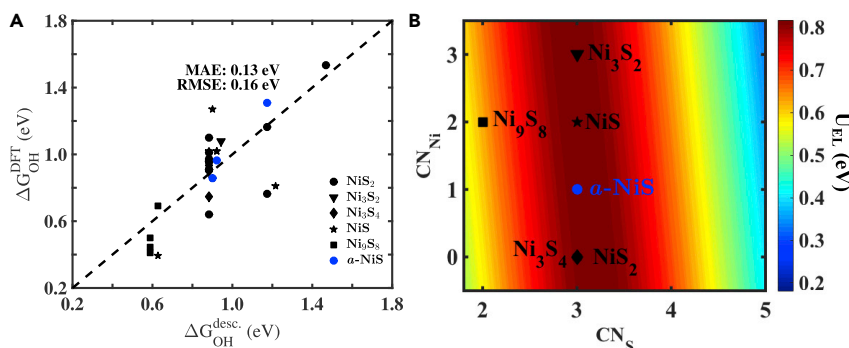


Figure 5. Structure-Energy-Activity Descriptor Based on Local Geometry

(A) Correlation between DFT-calculated free energy of adsorption of OH* and that obtained from the structure descriptor, based on the coordination numbers of the nearest-neighbor nickel and sulfur atoms. The dashed line represents perfect agreement between the structure descriptor and the DFT-computed ΔG_{OH} .

(B) Structure-activity contour plot of the expected limiting potential, U_{EL} , based on the structure descriptor, $\Delta G_{\text{OH}} = 0.29(0.08\text{CN}_{(\text{Ni})} + \text{CN}_{(\text{S})})$, from the coordination numbers of the nearest-neighbor nickel and sulfur atoms. The markers are plotted based on the local coordination around the active site for the various Ni-S phases. All the highly active phases exhibit active sites with three nearest-neighbor sulfur atoms albeit with different number of nickel neighbors.

involving all the calculated surface sites. We find, quite remarkably, a structure-energy descriptor relation: $\Delta G_{\text{OH}} = 0.29(\text{CN}_S + 0.08\text{CN}_{\text{Ni}})$, which has a mean absolute error of 0.13 eV (Figure 5A); the uncertainty in the descriptor is represented in Figures S19 and S20. This relation shows that the strong covalent Ni-S bonding affects OH* adsorption much more than the weak Ni-Ni metallic bonding. Therefore, to a first approximation, a simple geometric counting of S neighbors around the Ni surface site provides a measure of the ORR activity.

Using this relation, we can rephrase the challenge of finding active ORR catalysts into finding surface sites that have optimal local coordination. Our analysis suggests that having three sulfur atoms bonded to the active site leads to high activity (Figures S21 and S20). Remarkably, all the most active nickel sulfide (Figure 4B) phases possess this local coordination environment (Figure 5B), albeit with different Ni nearest neighbors, highlighting the robustness of the simple structure-energy-activity descriptor identified here. To further validate and probe the local effect, we considered adsorption on an amorphous structure (Figure 4C) with a composition of Ni:S 1.0:1.0, prepared through simulated annealing. We find that the same structure-energy descriptor based on the local environment determines the activity of sites on the amorphous structure (Table S2) with an average prediction error within the uncertainty of DFT-calculated binding energies.

This analysis suggests that surface sites, with suitable local coordination, can lead to high electrocatalytic activity and that several nickel sulfide phases possess such surface sites. These results imply that oxidative surface transformation of Ni_3S_2 serves to generate persistent, active Ni sites bonded to three sulfur atoms, which support high ORR activity. The identification of simple structure-energy-activity descriptors allows for the rapid identification of candidate materials and can accelerate the discovery of Pt-free electrocatalysts for ORR. Given the rich surface dynamics present under electrochemical conditions, the identification of structure-energy-activity descriptors allows for a robust estimate of the activity of the non-equilibrium surface structures that persist under reaction conditions.

Conclusions

We have established that Ni_3S_2 undergoes an *in situ* oxidative self-limiting surface reconstruction under the conditions of ORR catalysis in neutral aqueous electrolytes. This reconstruction serves to generate an approximately 2 nm conformal amorphous surface film with an approximate Ni:S ratio of 1:1. The surface-restructured Ni_3S_2 exhibits similar ORR activity to independently electrodeposited NiS phases, indicating that the reconstructed surface provides the active sites for ORR catalysis. DFT calculations reveal that the OH^* adsorption energy (ΔG_{OH^*}) on the a-NiS surface phase reflects the distribution in local coordination environments at surface-exposed Ni sites. Using an array of crystalline model structures, we have developed, for the first time, a coordination chemistry descriptor for ORR activity on nickel sulfide materials, which highlights the key role of the local coordination environment of the active site. This coordination chemistry descriptor, combined with knowledge of the pathways for surface reconstruction, provides a refined paradigm for designing earth-abundant catalysts that emphasizes the search for materials whose surfaces can serve as precatalysts that reconstruct to generate optimally coordinated active sites for ORR.

EXPERIMENTAL PROCEDURES

Bulk Ni_3S_2 Synthesis

Phase-pure Ni_3S_2 was prepared by solid-state synthesis.²⁶ Ni powder (15 mmol, 0.88 g) and S pieces (10 mmol, 0.32 g) were thoroughly mixed and ground in a mortar and pestle. The mixture was sealed under vacuum inside a quartz tube and heated for 24 hr at 600°C followed by 4 hr at 800°C. The resulting product was cooled to room temperature, ground to a fine powder first by mortar and pestle and then ball milled for 1 hr. The Ni_3S_2 electrode was prepared by casting 50 μL of a 10 mg mL^{-1} Ni_3S_2 suspension in ethanol onto an Au RDE to fully cover the Au surface. After drying in air, the electrode was pressed by a pellet press to obtain a flat surface of Ni_3S_2 .

Ni_3S_2 Nanoparticle Synthesis

To a 50 mL three-neck flask, 200 mg nickel(II) 2,4-pentanedionate and 10 mL 1,5-pentanediol were added. Under stirring, a solution of 75.9 mg cystamine dihydrochloride in 10 mL of 1,5-pentanediol was added to the nickel solution. The resulting mixture was degassed with N_2 and heated under N_2 reflux for 30 min. After cooling to room temperature, the suspended material was isolated via centrifugation at 5,000 rpm for 5 min. The crude product was then washed twice using 5 mL of 2-propanol and then twice with 5 mL of acetone. In each washing step, the sample was re-suspended with a vortex mixer and re-isolated via centrifugation at 5,000 rpm for 5 min. The product was then dried in air at 60°C for 3 hr and stored in the glovebox.³¹

NiS Film Electrodeposition

Fifty milliliters of 0.1 M $\text{NiCl}_2 \cdot 6\text{H}_2\text{O}$ solution was mixed with 10 mL of 0.1 M aqueous solution of D-(–)-tartaric acid and stirred for 20 min. Then, 25 mL of 0.1 M thioacetamide solution was added and stirred for an additional 10 min. The final volume of the solution was adjusted to 100 mL with water. The pH of this working solution was maintained at 5.5 by adding 28% ammonium hydroxide solution. A polished Au RDE was used as the substrate and working electrode and, together with a Pt mesh counter electrode and an Ag/AgCl reference electrode, an electrochemistry cell was constructed. Consecutive CV scans from –0.38 to 0.72 V versus RHE were performed at a scan rate of 5 mV s^{-1} . During the deposition, the working electrode was rotated at 600 rpm and the solution was continuously bubbled with N_2 . After 10 cycles, the Au RDE working electrode was removed from the deposition bath, gently washed with a copious amount of MilliQ water, and dried at room temperature in air. The as-prepared NiS films were annealed at 250°C for 3 hr in an N_2 atmosphere.^{32,33}

Physical Characterization

XRD, XPS, SEM, TEM, and EDS were conducted to reveal the composition, phase, morphology, and structure of each material under investigation (see [Supplemental Experimental Procedures](#) for further details).

Electrochemical Characterizations

CV, CA, and potentiostatic Tafel data were collected using a Biologic VSP 16-channel potentiostat or a Gamry Reference 600 potentiostat (see [Supplemental Experimental Procedures](#) for further details).

Computation

DFT calculations were performed using GPAW⁶² with the BEEF-vdW exchange correlation functional⁶³ using the Atomic Simulation Environment (ASE).⁶³ Core electrons were described using the Projector Augmented Wave Function (PAW), and k points were represented using Monkhorst Pack grids. All calculations were performed with a grid spacing of 0.18 Å and converged with a force criterion of <0.05 eV/Å. A 6 × 6 × 1 k-point grid was used for a unit cell having 3 atoms each in the x and y directions and with 4 layers in the z direction. The bottom two layers were fixed and the remaining layers were allowed to be relaxed. The free energies of oxygen intermediates were calculated using DFT, under standard conditions and at a potential of 0 V versus RHE by incorporating entropy contributions and zero-point energy. The effect of potential, U, is included by shifting the free energy of an electron by -eU.

SUPPLEMENTAL INFORMATION

Supplemental Information includes Supplemental Experimental Procedures, 27 figures, 3 tables, and 1 data file and can be found with this article online at <http://dx.doi.org/10.1016/j.joule.2017.08.020>.

AUTHOR CONTRIBUTIONS

B.Y. and D.K. contributed equally. Y.S. and B.Y. conceived of and designed the experimental investigations. B.Y. performed the experiments. V.V., D.K., C.H.H., and S.D. conceived of and designed the computational investigations. D.K., C.H.H., and S.D. performed the computations. Y.S., V.V., B.Y., D.K., and C.H.H. analyzed the data and wrote the paper.

ACKNOWLEDGMENTS

We gratefully acknowledge Dr. Shoji Hall, Anna Wuttig, Youngmin Yoon, and R. Soyoung Kim for helpful discussions. We gratefully acknowledge Dr. Yong Zhang for assistance with HRTEM data collection. The experimental portion of this work was supported by the NSF under award CHE-1454060, and by the MIT Department of Chemistry through junior faculty funds for Y.S. This work made use of the MRSEC Shared Experimental Facilities at MIT, which is supported in part by the NSF under award DMR-0819762. The computational portion of this work was supported by NSF under award CBET-1554273. This work used the Extreme Science and Engineering Discovery Environment (XSEDE), which is supported by National Science Foundation grant number ACI-1548562.

Received: June 9, 2017

Revised: August 2, 2017

Accepted: August 30, 2017

Published: September 27, 2017

REFERENCES

1. Lewis, N.S., and Nocera, D.G. (2006). Powering the planet: chemical challenges in solar energy utilization. *Proc. Natl. Acad. Sci. USA* **103**, 15729–15735.
2. Katsounaros, I., Cherevko, S., Zeradjanin, A.R., and Mayrhofer, K.J.J. (2014). Oxygen electrochemistry as a cornerstone for sustainable energy conversion. *Angew. Chem. Int. Ed.* **53**, 102–121.
3. Matsumoto, Y., and Sato, E. (1986). Electrocatalytic properties of transition metal oxides for oxygen evolution reaction. *Mater. Chem. Phys.* **14**, 397–426.
4. Gasteiger, H.A., Kocha, S.S., Sompalli, B., and Wagner, F.T. (2005). Activity benchmarks and requirements for Pt, Pt-alloy, and non-Pt oxygen reduction catalysts for PEMFCs. *Appl. Catal. B Environ.* **56**, 9–35.
5. Kanan, M.W., and Nocera, D.G. (2008). In situ formation of an oxygen-evolving catalyst in neutral water containing phosphate and Co^{2+} . *Science* **321**, 1072–1075.
6. Long, X., Li, J., Xiao, S., Yan, K., Wang, Z., Chen, H., and Yang, S. (2014). A strongly coupled graphene and FeNi double hydroxide hybrid as an excellent electrocatalyst for the oxygen evolution reaction. *Angew. Chem. Int. Ed.* **126**, 7714–7718.
7. Gao, M.-R., Jiang, J., and Yu, S.-H. (2012). Solution-based synthesis and design of late transition metal chalcogenide materials for oxygen reduction reaction (ORR). *Small* **8**, 13–27.
8. Gao, M.-R., Xu, Y.-F., Jiang, J., and Yu, S.-H. (2013). Nanostructured metal chalcogenides: synthesis, modification, and applications in energy conversion and storage devices. *Chem. Soc. Rev.* **42**, 2986.
9. Helm, L., and Merbach, A.E. (2005). Inorganic and bioinorganic solvent exchange mechanisms. *Chem. Rev.* **105**, 1923–1959.
10. Helm, L., and Merbach, A.E. (1999). Water exchange on metal ions: experiments and simulations. *Coord. Chem. Rev.* **187**, 151–181.
11. Yeo, B.S., and Bell, A.T. (2011). Enhanced activity of gold-supported cobalt oxide for the electrochemical evolution of oxygen. *J. Am. Chem. Soc.* **133**, 5587–5593.
12. Lee, S.W., Carlton, C., Risch, M., Surendranath, Y., Chen, S., Furutsuki, S., Yamada, A., Nocera, D.G., and Shao-Horn, Y. (2012). The nature of lithium battery materials under oxygen evolution reaction conditions. *J. Am. Chem. Soc.* **134**, 16959–16962.
13. Trotochaud, L., Young, S.L., Ranney, J.K., and Boettcher, S.W. (2014). Nickel–iron oxyhydroxide oxygen-evolution electrocatalysts: the role of intentional and incidental iron incorporation. *J. Am. Chem. Soc.* **136**, 6744–6753.
14. Toda, T. (1999). Enhancement of the electroreduction of oxygen on Pt alloys with Fe, Ni, and Co. *J. Electrochem. Soc.* **146**, 3750.
15. Stamenkovic, V.R., Fowler, B., Mun, B.S., Wang, G., Ross, P.N., Lucas, C.A., and Marković, N.M. (2007). Improved oxygen reduction activity on $\text{Pt}_3\text{Ni}(111)$ via increased surface site availability. *Science* **315**, 493–497.
16. Alonso-Vante, N., Borthen, P., Fieber-Erdmann, M., Strehblow, H.-H., and Holub-Krappe, E. (2000). An in situ grazing incidence X-ray absorption study of ultra thin Ru_{x}Se_y cluster-like electrocatalyst layers. *Electrochim. Acta* **45**, 4227–4236.
17. Baresel, D., Von Sarholz, W., Schaarer, P., and Schmitz, J. (1974). Übergangs-Metallchalcogenide als Sauerstoff-Katalysatoren für Brennstoffzellen. *Ber. Bunsen-Ges.* **78**, 608–611.
18. Behret, H., Binder, H., and Sandstede, G. (1975). Electrocatalytic oxygen reduction with thiospinels and other sulphides of transition metals. *Electrochim. Acta* **20**, 111–117.
19. Feng, Y., Gago, A., Timperman, L., and Alonso-Vante, N. (2011). Chalcogenide metal centers for oxygen reduction reaction: activity and tolerance. *Electrochim. Acta* **56**, 1009–1022.
20. Susac, D., Sode, A., Zhu, L., Wong, P.C., Teo, M., Bizzotto, D., Mitchell, K.A., Parsons, R.R., and Campbell, S.A. (2006). A methodology for investigating new nonprecious metal catalysts for PEM fuel cells. *J. Phys. Chem. B* **110**, 10762–10770.
21. Falkowski, J.M., Concannon, N.M., Yan, B., and Surendranath, Y. (2015). Heazlewoodite, Ni_3S_2 : a potent catalyst for oxygen reduction to water under benign conditions. *J. Am. Chem. Soc.* **137**, 7978–7981.
22. Cheng, S., Liu, H., and Logan, B.E. (2006). Power densities using different cathode catalysts (Pt and CoTMPP) and polymer binders (Nafion and PTFE) in single chamber microbial fuel cells. *Environ. Sci. Technol.* **40**, 364–369.
23. Zhao, F., Harnisch, F., Schröder, U., Scholz, F., Bogdanoff, P., and Herrmann, I. (2005). Application of pyrolysed iron(II) phthalocyanine and CoTMPP based oxygen reduction catalysts as cathode materials in microbial fuel cells. *Electrochim. Comm.* **7**, 1405–1410.
24. Yan, B., Concannon, N.M., Milshtein, J.D., Brushett, F.R., and Surendranath, Y. (2017). A membrane-free neutral pH formate fuel cell enabled by a selective nickel sulfide oxygen reduction catalyst. *Angew. Chem. Int. Ed.* **56**, 7496–7499.
25. Bugajski, J., Gajda, T., Lemire, R.J., and Preis, W. (2004). *Chemical Thermodynamics of Nickel* (Elsevier).
26. Tare, V.B., and Wagner, J.B. (1983). Electrical conduction in two-phase nickel oxide-nickel sulfide mixtures. *J. Appl. Phys.* **54**, 252–257.
27. Fleet, M.E. (1977). The crystal structure of heazlewoodite, and metallic bonds in sulfide minerals. *Am. Mineral.* **62**, 341–345.
28. Buckley, A.N., and Woods, R. (1991). Electrochemical and XPS studies of the surface oxidation of synthetic heazlewoodite (Ni_3S_2). *J. Appl. Electrochem.* **21**, 575–582.
29. Casella, I.G., Guascito, M.R., and Sannazzaro, M.G. (1999). Voltammetric and XPS investigations of nickel hydroxide electrochemically dispersed on gold surface electrodes. *J. Electroanal. Chem.* **462**, 202–210.
30. Han, S.-C., Kim, H.-S., Song, M.-S., Lee, P.S., Lee, J.-Y., and Ahn, H.-J. (2003). Electrochemical properties of NiS as a cathode material for rechargeable lithium batteries prepared by mechanical alloying. *J. Alloys Compd.* **349**, 290–296.
31. Chi, W.S., Han, J.W., Yang, S., Roh, D.K., Lee, H., and Kim, J.H. (2012). Employing electrostatic self-assembly of tailored nickel sulfide nanoparticles for quasi-solid-state dye-sensitized solar cells with Pt-free counter electrodes. *Chem. Commun. (Camb.)* **48**, 9501–9503.
32. Jana, S., Samai, S., Mitra, B.C., Bera, P., and Mondal, A. (2014). Nickel oxide thin film from electrodeposited nickel sulfide thin film: peroxide sensing and photo-decomposition of phenol. *Dalton Trans.* **43**, 13096–13104.
33. Sun, Y., Liu, C., Grauer, D.C., Yano, J., Long, J.R., Yang, P., and Chang, C.J. (2013). Electrodeposited cobalt-sulfide catalyst for electrochemical and photoelectrochemical hydrogen generation from water. *J. Am. Chem. Soc.* **135**, 17699–17702.
34. Nørskov, J.K., Rossmeisl, J., Logadottir, A., and Lindqvist, L. (2004). Origin of the overpotential for oxygen reduction at a fuel-cell cathode. *J. Phys. Chem. B* **108**, 17886–17892.
35. Gauthier, J.A., Dickens, C.F., Chen, L.D., Doyle, A.D., and Nørskov, J.K. (2017). Solvation effects for oxygen evolution reaction catalysis on IrO_2 (110). *J. Phys. Chem. C* **121**, 11455–11463.
36. He, Z.-D., Hanselman, S., Chen, Y.-X., Koper, M.T.M., and Calle-Vallejo, F. (2017). Importance of solvation for the accurate prediction of oxygen reduction activities of Pt-based electrocatalysts. *J. Phys. Chem. Lett.* **8**, 2243–2246.
37. Calle-Vallejo, F., Krabbe, A., and García-Lastra, J.M. (2017). How covalence breaks adsorption-energy scaling relations and solvation restores them. *Chem. Sci.* **8**, 124–130.
38. Thiel, P.A., and Madey, T.E. (1987). The interaction of water with solid surfaces: fundamental aspects. *Surf. Sci. Rep.* **7**, 211–385.
39. Limmer, D.T., Willard, A.P., Madden, P., and Chandler, D. (2013). Hydration of metal surfaces can be dynamically heterogeneous and hydrophobic. *Proc. Natl. Acad. Sci. USA* **110**, 4200–4205.
40. Henderson, M. (2002). The interaction of water with solid surfaces: fundamental aspects revisited. *Surf. Sci. Rep.* **46**, 1–308.
41. Abild-Pedersen, F., Greeley, J., Studt, F., Rossmeisl, J., Munter, T.R., Moses, P.G., Skúlason, E., Bligaard, T., and Nørskov, J.K. (2007). Scaling properties of adsorption energies for hydrogen-containing molecules on transition-metal surfaces. *Phys. Rev. Lett.* **99**, 4–7.
42. Montemore, M.M., and Medlin, J.W. (2014). A unified picture of adsorption on transition metals through different atoms. *J. Am. Chem. Soc.* **136**, 9272–9275.

43. Fu, Q., Cao, X., and Luo, Y. (2013). Identification of the scaling relations for binary noble-metal nanoparticles. *J. Phys. Chem. C* 117, 2849–2854.
44. Fernández, E.M., Moses, P.G., Toftelund, A., Hansen, H.A., Martínez, J.I., Abild-Pedersen, F., Kleis, J., Hinnemann, B., Rossmeisl, J., Bligaard, T., and Nørskov, J.K. (2008). Scaling relationships for adsorption energies on transition metal oxide, sulfide, and nitride surfaces. *Angew. Chem. Int. Ed.* 120, 4761–4764.
45. Shustorovich, E. (1986). Bond making and breaking on transition-metal surfaces: theoretical projections based on bond-order conservation. *Surf. Sci.* 176, L863–L872.
46. Bell, A.T., and Shustorovich, E. (1990). A comment on the analysis of CO hydrogenation using the BOC-MP approach. *J. Catal.* 121, 1–6.
47. Viswanathan, V., and Hansen, H.A. (2014). Unifying solution and surface electrochemistry: limitations and opportunities in surface electrocatalysis. *Top. Catal.* 57, 215–221.
48. Calle-Vallejo, F., Inoglu, N.G., Su, H.-Y., Martínez, J.I., Man, I.C., Koper, M.T.M., Kitchin, J.R., and Rossmeisl, J. (2013). Number of outer electrons as descriptor for adsorption processes on transition metals and their oxides. *Chem. Sci.* 4, 1245.
49. Man, I.C., Su, H.-Y., Calle-Vallejo, F., Hansen, H.A., Martínez, J.I., Inoglu, N.G., Kitchin, J., Jaramillo, T.F., Nørskov, J.K., and Rossmeisl, J. (2011). Universality in oxygen evolution electrocatalysis on oxide surfaces. *ChemCatChem* 3, 1159–1165.
50. Calle-Vallejo, F., and Koper, M.T.M. (2012). First-principles computational electrochemistry: achievements and challenges. *Electrochim. Acta* 84, 3–11.
51. Stephens, I.E.L., Bondarenko, A.S., Grønbjerg, U., Rossmeisl, J., and Chorkendorff, I. (2012). Understanding the electrocatalysis of oxygen reduction on platinum and its alloys. *Energy Environ. Sci.* 5, 6744.
52. Viswanathan, V., Hansen, H.A., Rossmeisl, J., and Nørskov, J.K. (2012). Universality in oxygen reduction electrocatalysis on metal surfaces. *ACS Catal.* 2, 1654–1660.
53. Viswanathan, V., Hansen, H.A., Rossmeisl, J., and Nørskov, J.K. (2012). Unifying the $2e^-$ and $4e^-$ reduction of oxygen on metal surfaces. *J. Phys. Chem. Lett.* 3, 2948–2951.
54. Krishnamurthy, D., Hansen, H.A., and Viswanathan, V. (2016). Universality in nonaqueous alkali oxygen reduction on metal surfaces: implications for Li-O₂ and Na-O₂ batteries. *ACS Energy Lett.* 1, 162–168.
55. Wellendorff, J., Lundgaard, K.T., Møgelhøj, A., Petzold, V., Landis, D.D., Nørskov, J.K., Bligaard, T., and Jacobsen, K.W. (2012). Density functionals for surface science: exchange-correlation model development with Bayesian error estimation. *Phys. Rev. B* 85, 235149.
56. Deshpande, S., Kitchin, J.R., and Viswanathan, V. (2016). Quantifying uncertainty in activity volcano relationships for oxygen reduction reaction. *ACS Catal.* 6, 5251–5259.
57. Calle-Vallejo, F., Tymoczko, J., Colic, V., Vu, Q.H., Pohl, M.D., Morgenstern, K., Loffreda, D., Sautet, P., Schuhmann, W., and Bandarenka, A.S. (2015). Finding optimal surface sites on heterogeneous catalysts by counting nearest neighbors. *Science* 350, 185–189.
58. Calle-Vallejo, F., Loffreda, D., Koper, M.T.M., and Sautet, P. (2015). Introducing structural sensitivity into adsorption-energy scaling relations by means of coordination numbers. *Nat. Chem.* 7, 403–410.
59. Jackson, A., Viswanathan, V., Forman, A.J., Larsen, A.H., Nørskov, J.K., and Jaramillo, T.F. (2014). Climbing the activity volcano: core-shell Ru@Pt electrocatalysts for oxygen reduction. *ChemElectroChem* 1, 67–71.
60. Friebel, D., Viswanathan, V., Miller, D.J., Anniyev, T., Ogasawara, H., Larsen, A.H., O'Grady, C.P., Nørskov, J.K., and Nilsson, A. (2012). Balance of Nanostructure and bimetallic interactions in Pt model fuel cell catalysts: *in situ* XAS and DFT study. *J. Am. Chem. Soc.* 134, 9664–9671.
61. Fung, V., Tao, F.F., and Jiang, D. (2017). General structure-reactivity relationship for oxygen on transition-metal oxides. *J. Phys. Chem. Lett.* 8, 2206–2211.
62. Mortensen, J.J., Hansen, L.B., and Jacobsen, K.W. (2005). Real-space grid implementation of the projector augmented wave method. *Phys. Rev. B* 71, 35109.
63. Bahn, S.R., and Jacobsen, K.W. (2002). An object-oriented scripting interface to a legacy electronic structure code. *Comput. Sci. Eng.* 4, 56–66.